IEEE Photonics Journal
An IEEE Photonics Society Publication

Open Access

Transmission Properties of Fabry–Pérot Filter Consisting of Silicon-Based High-Contrast Gratings

Volume 8, Number 1, February 2016

Wei Wang
Xumin Gao
Xiaojing Fang
Xin Li
Hongbo Zhu
Yongjin Wang

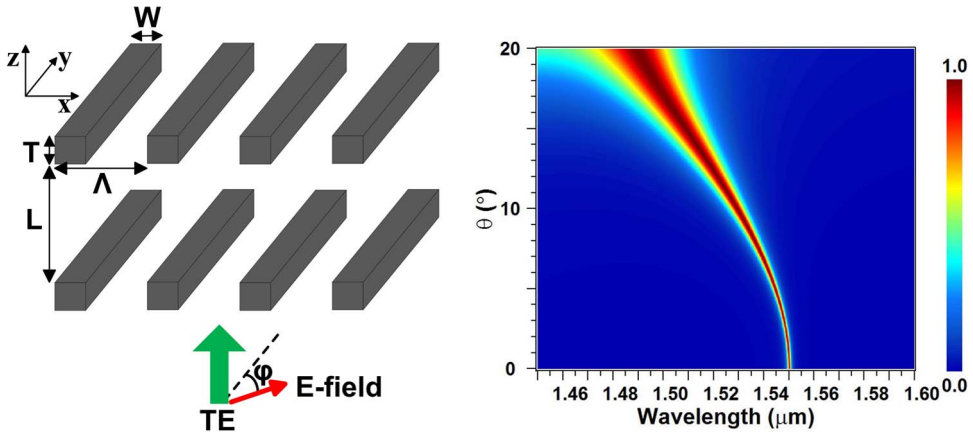

DOI: 10.1109/JPHOT.2015.2509867
1943-0655 © 2015 IEEE

IEEE photonics SOCIETY

IEEE

Transmission Properties of Fabry–Pérot Filter Consisting of Silicon-Based High-Contrast Gratings

Wei Wang, Xumin Gao, Xiaojing Fang, Xin Li, Hongbo Zhu, and Yongjin Wang

Grünberg Research Center, Nanjing University of Posts and Telecommunications, Nanjing 210003, China

DOI: 10.1109/JPHOT.2015.2509867
1943-0655 © 2015 IEEE. Translations and content mining are permitted for academic research only. Personal use is also permitted, but republication/redistribution requires IEEE permission. See http://www.ieee.org/publications_standards/publications/rights/index.html for more information.

Manuscript received December 2, 2015; accepted December 12, 2015. Date of publication December 17, 2015; date of current version December 29, 2015. This work was supported in part by the National Science Foundation of China under Grant 11104147 and Grant 61322112 and in part by Research Projects NY211001, NY213015, NY214029, 15KJB510021, CXLX13_458, and BJ211026. Corresponding author: Y. Wang (e-mail: wangyj@njupt.edu.cn).

Abstract: In this paper, we design and theoretically investigate an ultracompact Fabry–Pérot filter (FPF) consisting of two silicon-based high-contrast gratings (HCGs). The filter is proposed for implemention on a double silicon-on-insulator (double-SOI) platform. By using the rigorous coupled wave analysis method, we examine and discuss the influences of various factors on the transmission properties of the filter. The location of the transmission peak is capable of being tuned efficiently by changing the grating period, thickness, duty cycle, or filter cavity length. An ultrahigh quality factor (e.g., as high as 625960) can be readily achieved by merely choosing the appropriate grating period or thickness. Moreover, with increasing silicon substrate thickness, the modulation effect of the substrate is capable of decomposing the transmission peak into a bundle of subpeaks. In addition, structural differences between the two HCGs may degrade the peak transmittivity severely. In a word, this paper is devoted to a systematic report on the particular transmission properties of the filter and, thus, provides a clear picture of its overall performance, which is highly important for its practical design and applications.

Index Terms: Gratings, subwavelength structures, nanostructures, theory and design, silicon nanophotonics.

1. Introduction

Fabry–Pérot filters (FPFs) formed on semiconductor substrates have been investigated extensively due to their significant applications in various fields including wavelength division multiplexing telecommunication systems [1]–[4], optical sensing [5], [6] and optical switching [7], [8]. Two parallel broadband mirrors with high reflectivity are essential to construct FPFs. Traditionally, both mirrors consist of semiconductor distributed Bragg reflectors (DBRs), structures formed by multiple layers of alternating quarter-wave stacks with periodic variation in refractive indices, such as SiO_2/Ta_2O_5 on Si substrate [4], GaAs/AlGaAs on GaAs substrate [3], [9], and InP/InGaAsP on InP substrate [10]. Their reflectivity and bandwidth depend mainly on the refractive-index contrast of the constituent materials and stack pairs. Because of epitaxial growth constraints, conventional combinations of DBR materials usually have small differences in the refractive indices, resulting in an inordinately large number of stack pairs to achieve sufficiently high reflectivity, in addition to a

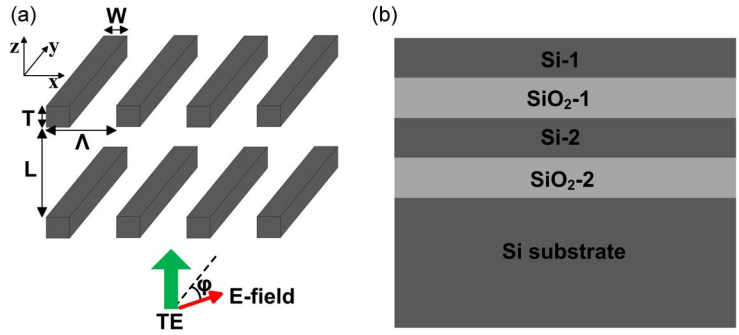

Fig. 1. (a) Schematic diagram of the silicon-based HCG-FPF. The green arrow shows the propagation direction of the incident light, while the red arrow denotes the E-field's direction. (b) Cross-sectional schematic diagram of the double-SOI platform.

small reflection bandwidth [11]. This has been a main challenge in the fabrication of compact, narrow full-width-at-half-maximum (FWHM), broadband FPFs. Although InP/air-gap DBRs seem to overcome the challenge to some extent, they are difficult to fabricate and, more importantly, prone to distortion and collapse [12], [13].

High-contrast gratings (HCGs), which consist of a high-index grating layer fully surrounded by low-index materials, have been proposed and demonstrated to overcome the limitations of conventional DBRs [14], [15]. By using only a single grating layer with thickness of hundreds of nanometers, HCGs can attain extraordinary and intriguing properties, such as high reflectivity, broad reflection band, and a small footprint, and thus, serve as high-quality mirrors in place of DBRs [16]–[18]. A kind of FPF composed of a top HCG mirror and a bottom DBR mirror has also been reported in [19] and theoretically investigated in [20]. HCGs reduce the mirror thickness, simplify the material growth requirements, and, thus, render relevant devices ultra-compact.

Complete replacement of the two DBRs with two HCGs in FPFs leads to HCG-based FPFs (HCG-FPFs), which feature ultra compactness, low weight, and the consequent potential of ultrafast tuning speed. Zhao *et al.* constructed an HCG-FPF with two layers of cross-stacked gratings but simply analyzed the resonant modes in the filter cavity [21]. Ho *et al.* proposed an HCG-FPF formed by two parallel 2-D HCGs with circular air-hole patterns [22], and recently implemented a similar structure monolithically on silicon substrate [23], whereas they mainly concentrated on the interesting experimental aspects. Thus far, few publications have provided a systematic report on the particular transmission properties of the HCG-FPFs, hindering our comprehensive understanding of this kind of filters. To fill the void, we present herein the design and analysis of a monolithic silicon-based HCG-FPF, which is proposed for implementation on a double silicon-on-insulator (double-SOI) platform. We first propose its feasible fabrication process. Then, various factors affecting its transmission properties are analyzed and discussed exhaustively by using the rigorous coupled wave analysis (RCWA) method. Our analysis makes the peculiar transmission properties of the filter more distinct, and hence provides a clear picture for the overall performance of the HCG-FPFs.

2. Design and Fabrication Process of the HCG-FPF

As shown in Fig. 1(a), the HCG-FPF consists of two parallel, identical, one-dimensional (1D) silicon-based HCGs, whose bars are periodic in the *x*-direction. The high-index silicon bars with refractive index of 3.48 are freely suspended, and are surrounded by air as low-index material. The structure parameters include grating period Λ, grating thickness T, grating bar width W, and duty cycle D. D is defined as the ratio of W to Λ. L represents the cavity length, i.e., the distance between the two HCGs. φ is the polarization angle. When the electric field (E-field) of the incident light is parallel to the grating bars ($\varphi = 0°$), we define it as TE polarization; when the E-field is perpendicular to the grating bars ($\varphi = 90°$), we define it as TM polarization. This HCG-FPF is proposed to be

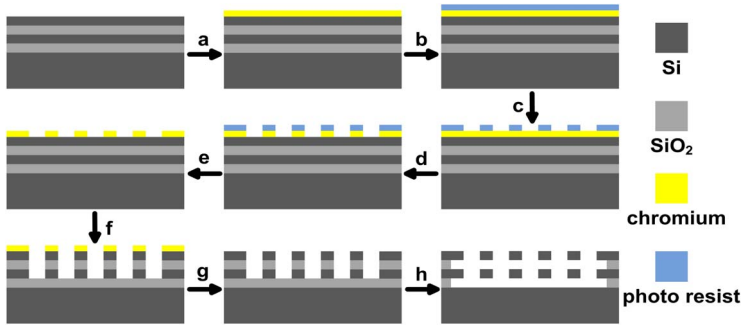

Fig. 2. Proposed fabrication flow of the silicon-based HCG-FPF on the double SOI-platform.

monolithically implemented on a double-SOI platform, the preparation process of which has been explicitly shown in [24]. As presented in Fig. 1(b), the double-SOI platform comprises two pairs of Si/SiO_2. Si-1 and Si-2 are the grating layers for the top and bottom HCGs, respectively, and have the same film thickness. SiO_2-1 acts as the filter cavity layer, whereas SiO_2-2 isolates the HCG-FPF from the bulk silicon substrate.

We scheme the flow of the feasible fabrication process, as shown in Fig. 2. First, a chromium layer is deposited on the top surface of the double-SOI platform (step a), followed by a spin-coated positive electron beam (EB) resist (step b). The resist film is exposed by using EB lithography equipment. After the development of the EB resist (step c), grating patterns are transferred to the chromium layer by using ion beam etching (IBE) technology (step d). Then, the EB resist is completely removed (step e), leaving the patterned chromium layer as a hard mask. In the following process, inductively coupled plasma (ICP) etching is used to transfer the grating structure to the layers of Si-1 and Si-2, and reactive ion etching (RIE) is used to transfer the grating structure to the layer of SiO_2-1 (step f). After the removal of chromium mask layer (step g), the buried layers of SiO_2-1 and SiO_2-2 are finally etched away by using hydrofluoric acid vapor to obtain two free-standing HCGs (step h), generating the HCG-FPF.

It is important to note that the HCG-FPF can also be achieved by following the fabrication flow shown in [23], which has been firstly proposed and experimentally verified by Ho *et al.*

3. Structure Parameters of the Designed HCG-FPF

First, it should be noted that all the simulations in this study are based on the RCWA method. The silicon-based HCG can be regarded as a wavelength-dependent mirror. However, its reflectivity and reflection phase corresponding to each wavelength cannot be obtained merely by the relevant classic theory such as the transfer matrix method (TMM), because of the periodic distribution of the HCG structure. Therefore, the transmission properties of the HCG-FPF also cannot be calculated by the TMM, which has been extensively applied to uniformly distributed thin-film DBR-based FPFs [3], [4]. RCWA is an accurate solution of Maxwell's equations for the electromagnetic diffraction induced by grating structures. The accuracy of the achieved solution depends solely on the number of terms reserved in the space-harmonic expansions of the electromagnetic fields. RCWA is also a non-iterative and straightforward technique that is widely used for various grating structures [25].

The finite-difference time-domain (FDTD) and the finite element method (FEM) are two other powerful tools for dealing with the electromagnetic problems of the grating structures. As alternative methods of the RCWA, they can certainly be used to calculate the transmission properties of the HCG-FPF.

Due to the asymmetric 1-D nature of the HCG [11], the HCG-FPF can be designed for TE (or TM) polarization application by choosing appropriate structure parameters. In the following simulations, the parameters are set as $\Lambda = 1.08\ \mu$m, $T = 0.24\ \mu$m, $D = 0.40$, and $L = 1.042\ \mu$m. HCG exhibits a broad high-reflection band only for TE polarization, as presented in Fig. 3(a). Therefore,

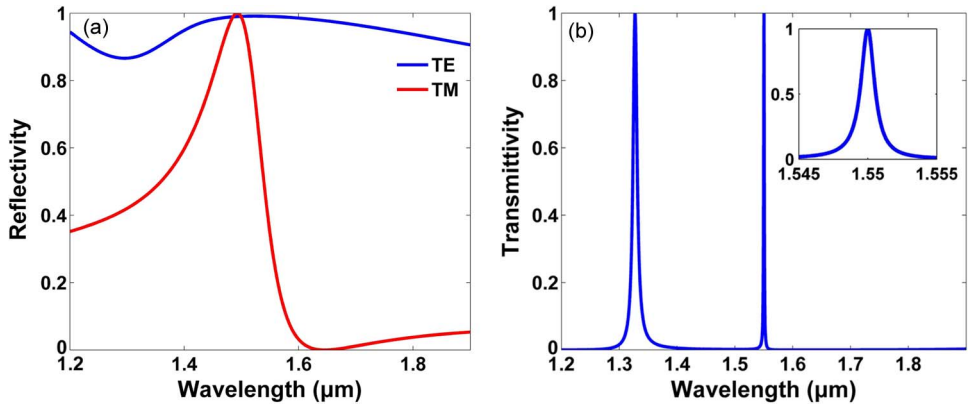

Fig. 3. (a) Reflection spectra of the HCG for TE and TM polarized lights, respectively. (b) Transmission spectrum of the HCG-FPF for TE polarized light. (Inset) Zoom-in peak located at 1.55 μm wavelength. Given the parameters $\Lambda = 1.08$ μm, $T = 0.24$ μm, $D = 0.40$, and $L = 1.042$ μm.

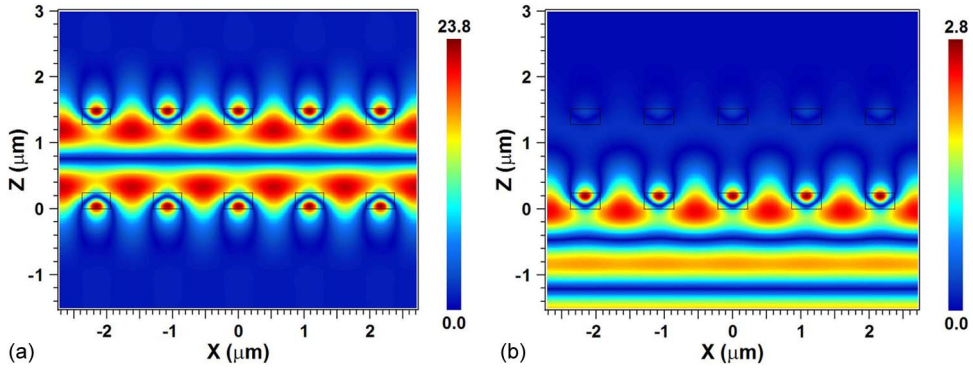

Fig. 4. Steady-state *E*-field distributions in and around the HCG-FPF for incident wavelengths of (a) 1.55 μm and (b) 1.50 μm. At 1.55 μm wavelength, field energy mainly builds up symmetrically in HCG-FPF due to strong Fabry–Pérot resonance; on the other hand, field energy is almost reflected back at 1.50 μm wavelength resulting from off resonance. The rectangles show the positions of the grating bars. The field intensities have been scaled according to the color bars, respectively.

this set of parameters is only suitable for TE polarization. Consequently, the following simulations are all based on surface normal incident TE polarized light unless specified. Fig. 3(b) shows the transmission spectrum of the HCG-FPF, in which a sharp peak is observed at 1.55 μm wavelength. Another peak at around 1.327 μm wavelength, arising from an adjacent resonant mode, has a broader FWHM due to the lower reflectivity of the HCG at the corresponding resonant wavelength. The distance between the two peaks shows a free spectrum range (FSR) of ~0.223 μm. In the following, we mainly focus on the transmission peak located within the most popular optical communication window, i.e., 1.55 μm wavelength. The inset of Fig. 3(b) shows the detail of the target peak at 1.55 μm wavelength, from which an FWHM of ~1.2 nm can be obtained, corresponding to a fineness of ~460 and a quality factor of ~1292.

Fig. 4 provides a view of the steady-state *E*-field distributions in and around the HCG-FPF. Blue indicates areas with low field intensity, while dark red denotes regions with high field intensity. In Fig. 4(a), for the incident wavelength of 1.55 μm, the buildup of field energy mainly emerges symmetrically in the grating bar regions and the filter cavity, which confirms that strong coupling between Fabry–Pérot modes and waveguide modes occurs in the HCG-FPF. Consequently, the field energy corresponding to 1.55 μm wavelength will transit through due to the Fabry–Pérot resonance. However, because of the much stronger enhancement of the field (as high as ~23.8 times) in the HCG-FPF, the incident and emergent field distributions cannot be distinctly observed in

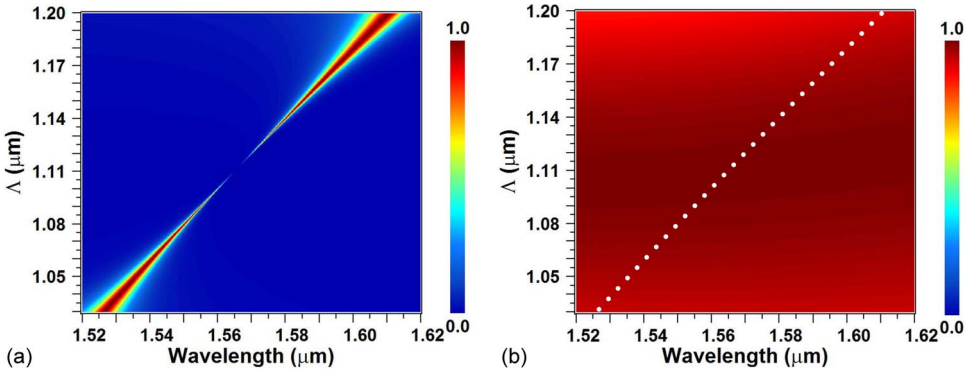

Fig. 5. (a) Transmission contour of the HCG-FPF and (b) the reflection contour of the HCG as functions of wavelength and grating period Λ, given the parameters $T = 0.24$ μm, $D = 0.40$, and $L = 1.042$ μm. The transmittivity of the HCG-FPF and the reflectivity of the HCG have been scaled according to the color bars, respectively. Dark red indicates areas with high transmittivity and dark blue denotes regions with low transmittivity in (a), while dark red shows the areas with high reflectivity in (b).

Fig. 4(a). For a comparison, electric field distribution for 1.50 μm wavelength is shown in Fig. 4(b), in which no obvious resonance is observed in the filter cavity. Thus, the incident field mainly interacts with the bottom HCG, and only guided mode resonance occurs. Under this circumstance, the HCG-FPF acts as a high reflectivity mirror, reflecting back the field energy. The reflected field interferes with the incident one, producing interference patterns.

4. Transmission Properties of the HCG-FPF

Several factors (including grating thickness, period, duty cycle, filter cavity length, oblique incident angle, and so on) may influence the transmission properties of the HCG-FPF. The effect of each factor is investigated in the succeeding sections.

4.1. Effect of the Grating Period Λ

Fig. 5(a) presents the transmission contour of the HCG-FPF as a function of wavelength and grating period Λ, given the parameters $T = 0.24$ μm, $D = 0.40$, and $L = 1.042$ μm; the figure shows how the transmission peak at around 1.55 μm wavelength evolves against Λ. With the increase in Λ, a quasi-linear red shift of the peak is observed, accompanied by an initial decrease and a subsequent increase in its FWHM. The red shift of the peak may be explained qualitatively as follows. At the transmission peak wavelength λ_0, the phase shift originated from a single round-trip of propagation in the filter cavity should be a multiple of 2π, which ensures the resonance condition inside the cavity. The total phase shift after a round-trip can be expressed as [26]

$$\Delta\varphi_{\text{HCG1}} + \Delta\varphi_{\text{cavity}} + \Delta\varphi_{\text{HCG2}} + \Delta\varphi_{\text{cavity}} = 2\ \text{m}\pi \tag{1}$$

where m is an integer; $\Delta\varphi_{\text{HCG1}}$, $\Delta\varphi_{\text{HCG2}}$, and $\Delta\varphi_{\text{cavity}}$ are the phase shifts imparted by the top HCG, the bottom HCG, and the filter cavity, respectively. Here, $\Delta\varphi_{\text{HCG1}}$ is equal to $\Delta\varphi_{\text{HCG2}}$ due to the identical structure of the two HCGs. $\Delta\varphi_{\text{HCG1}}$ $(\Delta\varphi_{\text{HCG2}})$ is very sensitive to the incident wavelength and structure parameters, such as Λ, T, and D. An in-depth study on this subject was carried out in [27]. When Λ varies, $\Delta\varphi_{\text{HCG1}}$ $(\Delta\varphi_{\text{HCG2}})$ also changes, and the established resonance condition is broken. Instead of passing through, the aforementioned wavelength λ_0 will be stopped. Hence, the incident wavelength has to shift until a new resonance condition is built, for instance, at λ_1. Thus, λ_1 will become the new transmission peak wavelength. In a word, the red shift of the peak here should be attributed to the phase shift variation of the HCG resulting from the increase in Λ. Corresponding to $\Lambda = 1.05$ μm, 1.08 μm, 1.11 μm, 1.14 μm, and 1.17 μm, the peak locations are calculated to be at 1.5356 μm, 1.5500 μm, 1.5648 μm, 1.5798 μm, and 1.5951 μm, respectively. The

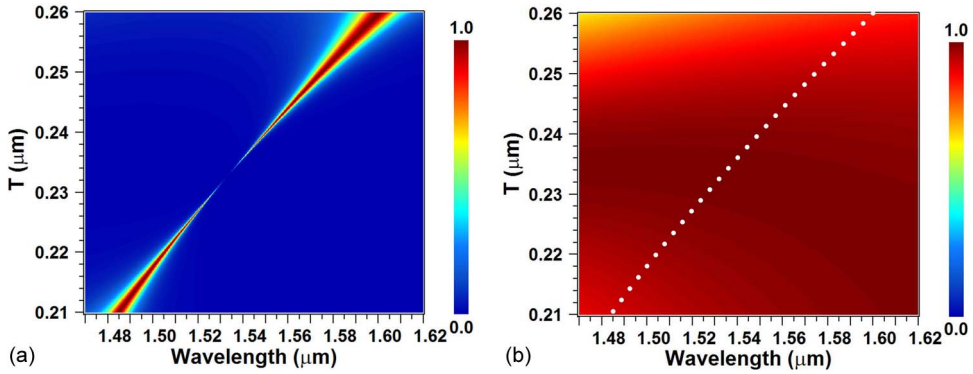

Fig. 6. (a) Transmission contour of the HCG-FPF and (b) the reflection contour of the HCG as functions of wavelength and grating thickness T, given the parameters $\Lambda = 1.08$ μm, $D = 0.40$, and $L = 1.042$ μm.

wavelength intervals between adjacent peaks are 14.4 nm, 14.8 nm, 15.0 nm, and 15.3 nm, quantitatively verifying the quasi-linear relationship of the peak location against Λ.

For a DBR-based FPF, there is an inverse relationship between the FWHM and the DBR reflectivity; that is, the higher the DBR reflectivity is, the narrower the FWHM will be. When it comes to the HCG-FPF, the same situation exists. Fig. 5(b) shows the reflection contour of the HCG as a function of wavelength and Λ, with the white dotted line indicating the HCG reflectivity corresponding to the transmission peak in Fig. 5(a). The HCG reflectivity first increases and then decreases along the white dotted line for Λ values from 1.03 μm to 1.20 μm, which leads the FWHM of the transmission peak to behave in an opposite way, that is, first decreases and then increases, just as shown in Fig. 5(a). Most notably, when Λ is around 1.11 μm, the FWHM is so narrow due to the ultra-high (approaching 100%) HCG reflectivity that the peak seems to disappear from Fig. 5(a). For $\Lambda = 1.11$ μm, the transmission peak is located at 1.5648 μm wavelength, whereas the HCG reflectivity and FWHM are calculated to be 0.99998 and 0.0025 nm, respectively. The peak with such a narrow FWHM cannot be clearly observed in Fig. 5(a). On the other hand, the FWHM is inversely proportional to the quality factor of the HCG-FPF, i.e., $Q = \lambda/\text{FWHM}$, where Q and λ denote the value of the quality factor and the peak wavelength, respectively. Here, an FWHM of 0.0025 nm corresponds to a Q value as high as 625960. Λ is known to be a lithographically defined parameter and can be adjusted easily and continuously. In other words, the quality factor can be tuned continuously and an ultra-high Q value may also be achieved readily merely by changing Λ lithographically. This is much superior to DBR-based FPFs, in which an increasing quality factor requires inordinately additional DBR pairs. Finally, it should be pointed out that the theoretical peak transmittivity remains constant to unity during the whole process of increasing Λ from 1.03 μm to 1.20 μm.

4.2. Effect of the Grating Thickness T

Fig. 6(a) shows the transmission contour of the HCG-FPF as a function of wavelength and grating thickness T with the other structure parameters fixed at $\Lambda = 1.08$ μm, $D = 0.40$, and $L = 1.042$ μm. In pace with the increasing T, a quasi-linear red shift of the transmission peak is observed. The increasing T results in the alteration of $\Delta\varphi_{\text{HCG1}}$ $(\Delta\varphi_{\text{HCG2}})$; thus, the resonance condition expressed by (1) is broken. Therefore, the peak has to shift toward a longer wavelength at which (1) is fulfilled again. When $T = 0.21$ μm, 0.22 μm, 0.23 μm, 0.24 μm and 0.25 μm, the peaks are calculated to be at wavelengths of 1.4845 μm, 1.5049 μm, 1.5267 μm, 1.5500 μm, and 1.5747 μm, respectively. The wavelength intervals between adjacent peaks are 20.4 nm, 21.8 nm, 23.3 nm, and 24.7 nm, respectively, indicating the quasi-linear relationship of the peak location against T.

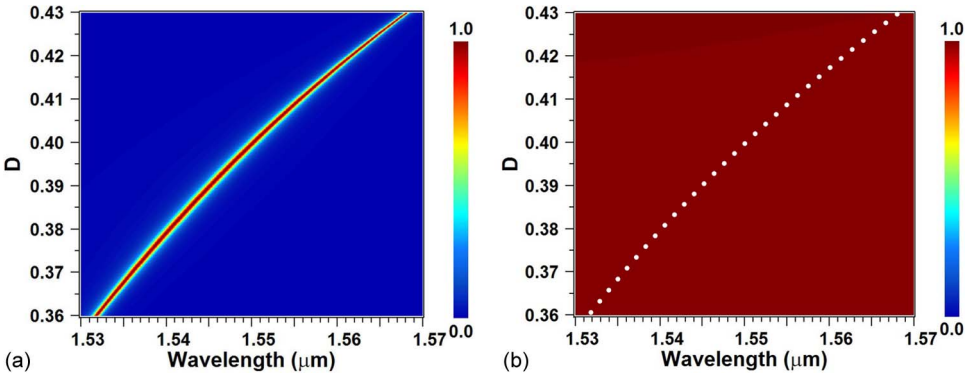

Fig. 7. (a) Transmission contour of the HCG-FPF and (b) the reflection contour of the HCG as functions of wavelength and duty cycle D, given the parameters $\Lambda = 1.08$ μm, $T = 0.24$ μm, and $L = 1.042$ μm.

Fig. 6(b) shows the reflection contour of the HCG as a function of wavelength and T, with the white dotted line indicating the HCG reflectivity corresponding to the transmission peak in Fig. 6(a). The FWHM of the peak in Fig. 6(a) first decreases and then increases, as a response to the variation of the HCG reflectivity indicated by the white dotted line in Fig. 6(b). Similarly to Fig. 5(a), when T is around 0.233 μm, the FWHM is so narrow due to the ultra-high HCG reflectivity that the peak is not observable in Fig. 6(a). At $T = 0.233$ μm, the peak is located at 1.5337 μm wavelength, whereas the HCG reflectivity and FWHM are 0.99998 and 0.0027 nm, respectively. The corresponding Q value is as high as 568037. Therefore, the FWHM of the peak, as well as the quality factor, can be readily tuned by varying T. Similarly, the theoretical peak transmittivity remains at 1 as T increases from 0.21 μm to 0.26 μm in Fig. 6(a).

4.3. Effect of the Grating Duty Cycle D

Fig. 7(a) presents the transmission contour of the HCG-FPF as a function of wavelength and duty cycle D, given the parameters $\Lambda = 1.08$ μm, $T = 0.24$ μm, and $L = 1.042$ μm; a red shift of the peak is observed as D increases. Similarly to increasing Λ and T, increasing D results in the variation of $\Delta\varphi_{\mathrm{HCG1}}$ and $\Delta\varphi_{\mathrm{HCG2}}$, which eventually leads the peak to a red shift. Compared with Figs. 5(a) and 6(a), Fig. 7(a) indicates a significant difference in that the FWHM of the peak varies much more moderately, mainly stemming from inconspicuous variation in HCG reflectivity along the white dotted line, as shown in Fig. 7(b).

4.4. Effect of the Cavity Length L

Fig. 8(a) presents the transmission contour of the HCG-FPF as a function of wavelength and cavity length L, given the parameters $\Lambda = 1.08$ μm, $T = 0.24$ μm, and $D = 0.40$. The peak moves from wavelengths 1.532 μm to 1.576 μm in a quasi-linear manner as L increases from 1.00 μm to 1.10 μm. Here, the peak shifting arises from the phase shift variation of the cavity rather than that of the HCG. By changing L, we can efficiently tune the transmission peak. This tuning mechanism has been widely implemented in DBR-based FPFs through thermal-optic [2] or micro-electro-mechanical system (MEMS) techniques [1], [13]. Furthermore, it seems that the FWHM of the peak almost keeps constant when L varies, as shown in Fig. 8(a), which implies a high uniformity of HCG reflectivity in the wavelength range of $1.53 \sim 1.58$ μm [see Fig. 3(a)]. At $L = 1.02$ μm, 1.04 μm, 1.06 μm, 1.08 μm, and 1.10 μm, Fig. 8(b) shows five transmission curves with peaks at wavelengths of 1.5408 μm, 1.5493 μm, 1.5580 μm, 1.5668 μm, and 1.5759 μm, respectively. Thus, the wavelength intervals between adjacent peaks are 8.5 nm, 8.7 nm, 8.8 nm, and 9.1 nm, quantitatively confirming the quasi-linear relationship of the peak location against L. Meanwhile, corresponding to each peak, the FWHM and the HCG reflectivity are calculated to be 1.1 nm, 1.1 nm, 1.2 nm, 1.3 nm, 1.5 nm, and 0.99078, 0.99038, 0.98983, 0.98914, 0.98828, respectively.

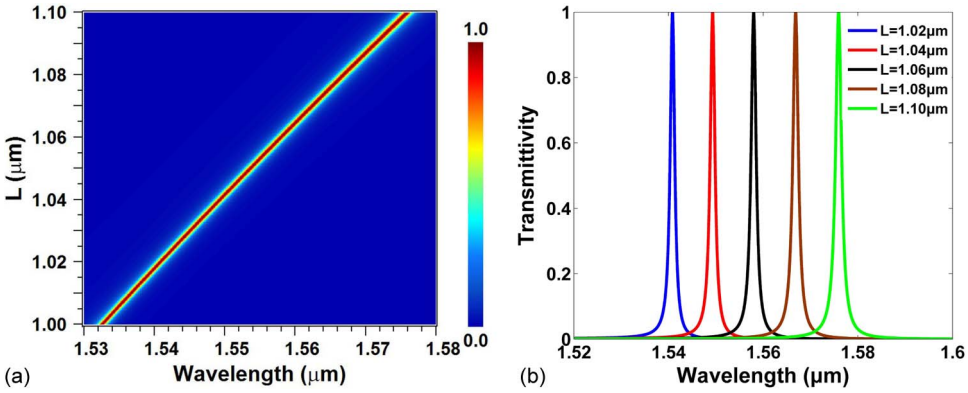

Fig. 8. (a) Transmission contour of the HCG-FPF as a function of wavelength and L. (b) Five transmission curves against wavelength with $L = 1.02$ μm, 1.04 μm, 1.06 μm, 1.08 μm, and 1.10 μm, respectively. Given parameters $\Lambda = 1.08$ μm, $T = 0.24$ μm, and $D = 0.40$.

Therefore, along with the increase in L, an inconspicuous broadening of the FWHM is observed in Fig. 8(a) as a response to the slight degradation in HCG reflectivity.

4.5. Effect of the Incident Beam Plane Angle

In this section, the effect of non-zero incident beam plane angle is considered. The incident beam plane angle is the angle of rotation of the HCG about the z-axis, and equal to the polarization angle φ defined in Fig. 1(a). The HCG-FPF here is designed only suitable for TE polarization, and its transmission performance will surely be affected by the non-zero incident beam plane angle φ. Fig. 9(a) presents the transmission contour of the HCG-FPF as a function of φ and wavelength, given the parameters $\Lambda = 1.08$ μm, $T = 0.24$ μm, $D = 0.40$, and $L = 1.042$ μm. A decrease in peak transmitivitty, as well as a rise in side-band, can be observed when φ increasing. This phenomenon is shown more intuitively in Fig. 9(b), which displays four transmission curves corresponding to $\varphi = 10°$, 20°, 30°, and 40°, respectively. To make the explanation to this phenomenon more understandable, we show the transmission curves of the HCG-FPF under TE-only $(\varphi = 0°)$ and TM-only $(\varphi = 90°)$ polarizations in Fig. 9(c) and (d), respectively. When φ is between 0° and 90°, the incident light E-field can be decomposed into two orthogonal parts, that is, TE component E_{TE} and TM component E_{TM}, since E-field is a vector. Therefore, the transmission curve of the HCG-FPF corresponding to a certain φ in Fig. 9(b) can be considered as a composition of the curves in Fig. 9(c) and (d) through a weighting factor, which is dominated by φ. With φ increasing, E_{TM} will increase, too; thus, the weight of Fig. 9(d) in the final transmission curve also increases. Consequently, the peak transmittivity of the HCG-FPF at 1.55 μm wavelength gradually decreases, whereas the side-band arises.

4.6. Effect of the Oblique Incident Angle

All the simulations in the front sections are carried out based on the rigid surface normal incidence; however, off-normal incidence may sometimes be closer to reality. In the following, we investigate the transmission properties of the HCG-FPF under oblique incident TE polarization. For simplicity, we assume that the incident plane is perpendicular to the grating bar direction, i.e., in the $x-z$ plane, as shown in Fig. 1(a). Fig. 10(a) presents the transmission contour of the HCG as a function of wavelength and incident angle θ, given the parameters $\Lambda = 1.08$ μm, $T = 0.24$ μm, $D = 0.40$, and $L = 1.042$ μm; a blue shift of the peak occurs in a nonlinear manner against θ, eventually forming a trumpet-shaped trajectory when θ from 0° to 20°. Oblique incidence decreases L_{eff} by $L_{eff} \sim L\cos\theta$ and consequently moves the peak toward a shorter wavelength. Here, L_{eff} denotes the effective cavity length of the HCG-FPF.

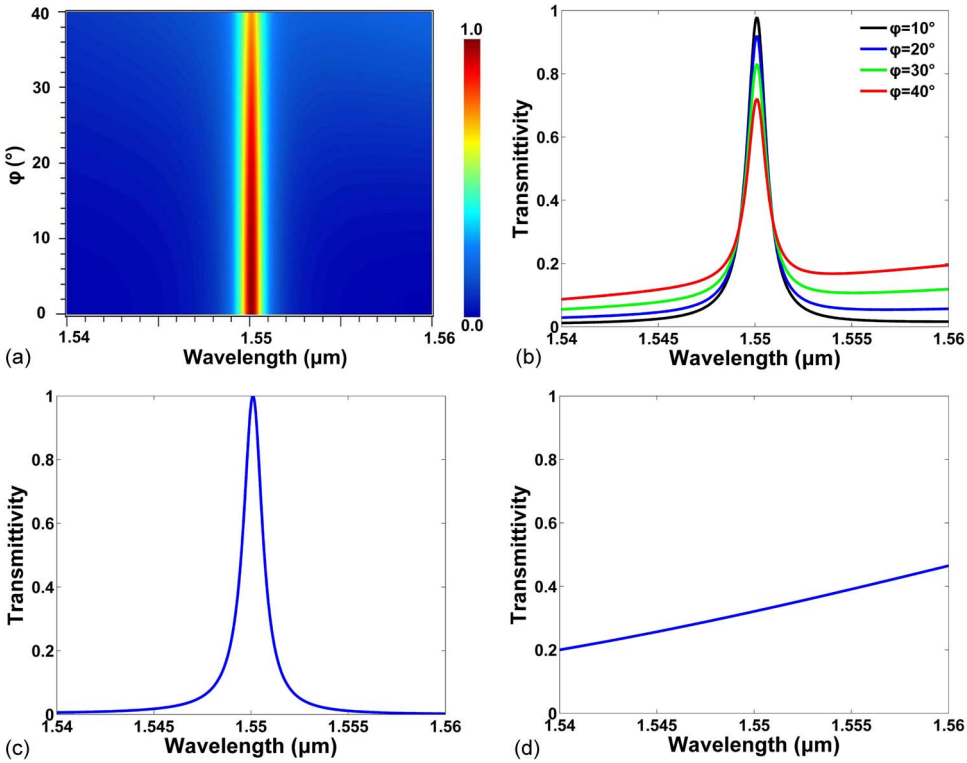

Fig. 9. (a) Transmission contour of the HCG-FPF as a function of wavelength and incident beam plane angle φ. (b) Simulated four transmission curves of the HCG-FPF corresponding to $\varphi = 10°$, 20°, 30°, and 40°, respectively; the transmission curves of the HCG-FPF under (c) TE-only and (d) TM-only polarizations, respectively. Given the parameters $\Lambda = 1.08$ μm, $T = 0.24$ μm, $D = 0.40$, and $L = 1.042$ μm.

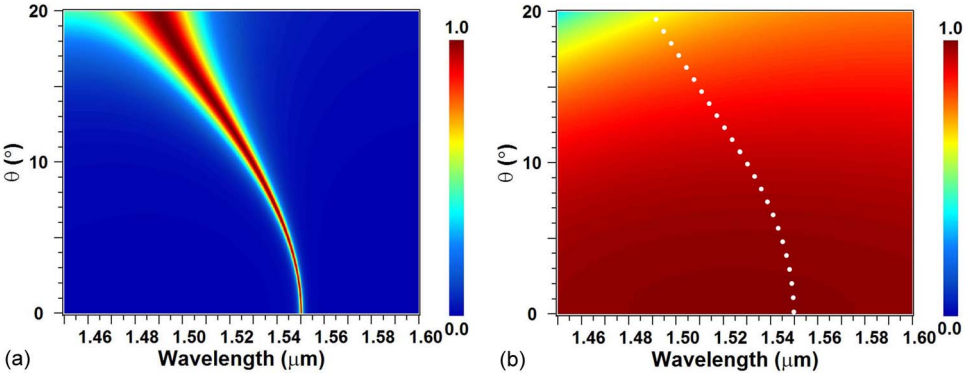

Fig. 10. (a) Transmission contour of the HCG-FPF and (b) the reflection contour of the HCG as functions of wavelength and incident angle θ, given the parameters $\Lambda = 1.08$ μm, $T = 0.24$ μm, $D = 0.40$, and $L = 1.042$ μm.

A simulation of the reflection contour of HCG versus wavelength and θ is shown in Fig. 10(b), in which the white dotted line indicates the HCG reflectivity corresponding to the transmission peak in Fig. 10(a). As θ increases, the FWHM of the peak broadens rapidly due to the obvious decrease in the HCG reflectivity along the white dotted line, which also means a severe degradation in the quality factor. However, both the peak location and the FWHM show a moderate

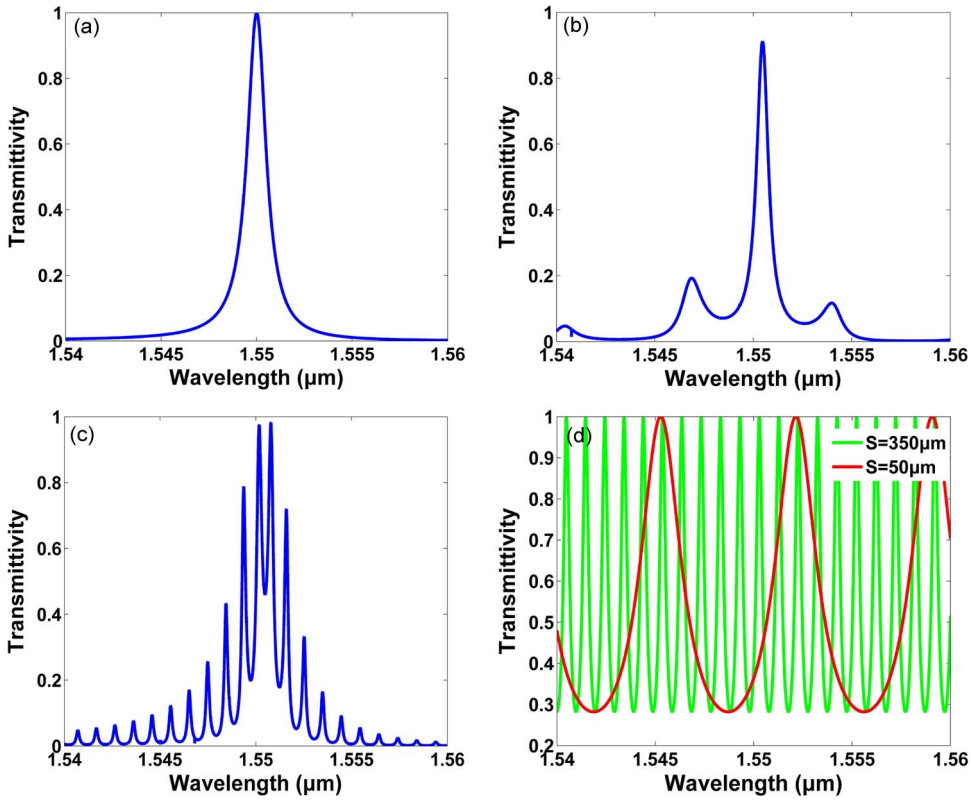

Fig. 11. Transmission spectra of the HCG-FPF with silicon substrate thickness S to be (a) 0 μm, (b) 50 μm, and (c) 350 μm, respectively. With S increasing, the transmission peak gradually deteriorates by splitting up. The thicker the substrate is, the worse the peak will be. (d) Transmission curves of the silicon substrate for $S = 50$ μm and 350 μm, respectively.

variation when θ is relatively small, e.g., $\theta < 3^\circ$, as shown in Fig. 10(a). Therefore, the oblique incident angle-dependent effect, to some extent, becomes insignificant in relation to a quasi-normal incidence as θ is small enough.

4.7. Effect of the Silicon Substrate

Thus far, we have not considered the influence of the silicon substrate. Because the proposed HCG-FPF is arranged on a double-SOI platform, we cannot neglect the existence of the substrate. Fig. 11(a)–(c) presents the transmission spectra of the HCG-FPF as a function of wavelength at $S = 0$ μm, 50 μm, and 350 μm, respectively, given the parameters $\Lambda = 1.08$ μm, $T = 0.24$ μm, $D = 0.40$, and $L = 1.042$ μm. S denotes substrate thickness. A perfect transmission peak is observed when the substrate is absent $(S = 0$ μm$)$, as shown in Fig. 11(a). For a relatively thin substrate $(S = 50$ μm$)$, as shown in Fig. 11(b), small side lobes begin to appear around the main peak. Along with the increase in S, the peak undergoes further deterioration. For $S = 350$ μm (a typical thickness for silicon substrate), as shown in Fig. 11(c), the main peak splits into a bundle of sub-peaks, which degrades the performance of the HCG-FPF severely. The substrate itself can practically be regarded as an FPF, which is with a low fineness due to the poor (around 30%) reflectivity at the silicon/air interface. The existence of the substrate imposes a strong modulation on the ideal spectrum of the HCG-FPF, causing the total spectrum to split up. For $S = 50$ μm and 350 μm, as shown in Fig. 11(d), the transmission spectra of the silicon substrate have modulation periods of ~7 nm and ~1 nm, respectively, which further verifies that a thicker substrate results in a stronger modulation.

Fig. 12(a) and (b) presents the transmission contour of the HCG-FPF as a function of wavelength and S, showing the modulation effect of the substrate on the transmission spectrum as S

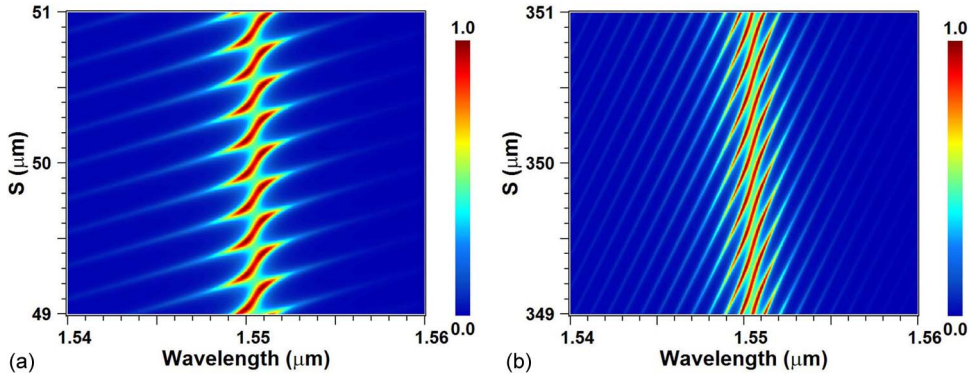

Fig. 12. Transmission contours of the HCG-FPF with the substrate thickness S (a) from 49 μm to 51 μm and (b) from 349 μm to 351 μm, respectively.

varies. When the substrate is relatively thin, i.e., around 50 μm, as shown in Fig. 12(a), only a few side lobes appear on both sides of the main peak, and their locations are closely dependent on the specific S value. Meanwhile, the main peak position also changes in a periodic manner as S varies. On the contrary, with a thick substrate of around 350 μm, as shown in Fig. 12(b), the peak decomposes into a heap of sub-peaks, the wavelength locations of which are also determined by S. A thinner substrate results in a better transmission spectrum.

A feasible way to suppress the sub-peaks is to reduce the substrate thickness as much as possible by well-controlled grinding and polishing. Another method is the complete removal of the silicon substrate from the backside by the deep reactive ion etching (DRIE) technique, which has been widely applied to the fabrication of various membrane devices on the GaN/Si platform [28], [29]. A third method is the deposition of an appropriate anti-reflection coating (ARC) layer aimed at 1.55 μm wavelength on the bottom silicon/air interface. ARC is a popular technique to diminish or even eliminate the reflection at an interface formed by a dielectric material and the air. With the aid of the ARC layer, the reflection at the bottom silicon/air interface will be significantly diminished, and thus, the FP cavity formed by the two silicon/air interfaces will be eliminated. Naturally, the modulation effect of the substrate will be considerably suppressed. According to the classic theory correlated to ARC, the refractive index n_{ARC} of an ideal ARC layer can be easily obtained as $n_{ARC} = (n_{Si} * n_{Air})^{1/2} \approx 1.865$, where n_{Si} and n_{Air} are the refractive indexes of the silicon substrate and air, respectively. HfO_2 may be a good choice for the ARC material. HfO_2 is transparent from the visible-to-infrared band and possesses outstanding characteristics, including a high laser damage threshold, and good thermal/chemical stability. Besides, an HfO_2 membrane can be efficiently prepared through several techniques, including atomic layer deposition and electronic beam evaporation [30]. The refractive index of HfO_2 at around 1.55 μm wavelength is generally within 1.8$\sim$2.05, which is highly correlated to the preparation technique and material quality.

4.8. Effect of the Structural Differences Between the Two HCGs

Previous simulations have assumed the two HCGs have identical structure parameters. Nevertheless, the proposed fabrication process, as shown in Fig. 2, may result in structural differences in grating thickness and duty cycle between the two HCGs. Here, we assume that the bottom HCG in Fig. 1(a) has grating period Λ_1, thickness T_1, and duty cycle D_1, whereas the top HCG has corresponding parameters of Λ_2, T_2, and D_2, respectively. The cavity length L is set at 1.042 μm, and the influence of the substrate $(S = 0)$ is neglected. Fig. 13(a) presents the transmission contour of the HCG-FPF as a function of wavelength and T_1, given the parameters $\Lambda_1 = \Lambda_2 = 1.08$ μm, $D_1 = D_2 = 0.40$, and $T_2 = 0.24$ μm; the figure shows the influence of fabrication deviations in thickness of the two HCGs. The peak moves as T_1 deviates from T_2, which is apprehensible considering (1). The alteration of the FWHM should be attributed to the

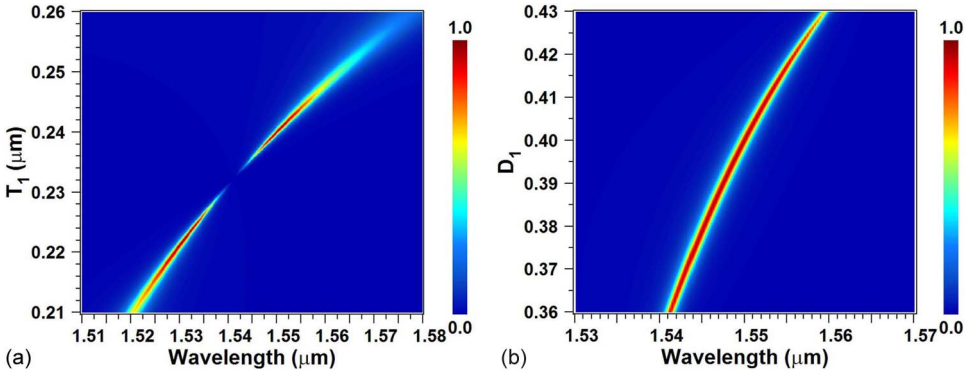

Fig. 13. Transmission contours of the HCG-FPF as functions of wavelength and (a) T_1 and (b) D_1. Structural differences between the two HCGs will change the FWHM and peak location and, particularly, degrade the peak transmittivity.

changes in the bottom HCG reflectivity, as discussed in the preceding sections. Most notably, increasing the deviation of T_1 from T_2 will tremendously degrade the peak transmittivity because the reflectivity imbalance between the two HCGs is deeply exacerbated [see Fig. 6(b)] [19]. Therefore, the consistency of T_1 with T_2 during the actual fabrication process should be sustained as much as possible because of the relatively small tolerance for the difference between them. Fig. 13(b) presents the transmission contour of the HCG-FPF as a function of wavelength and D_1, given the parameters $\Lambda_1 = \Lambda_2 = 1.08$ μm, $T_1 = T_2 = 0.24$ μm, and $D_2 = 0.40$. When D_1 deviates from D_2, the peak location, as well as its FWHM, changes. The deviation of D_1 from D_2 also leads to reflectivity imbalance between the two HCGs, which will degrade the peak transmittivity. Fig. 13(b) shows a much lesser degradation of the peak transmittivity in comparison with Fig. 13(a), indicating a relatively larger tolerance for the difference between D_1 and D_2.

5. Discussions

Through RCWA simulations, we show that the peak location of the HCG-FPF can be tuned efficiently by changing the grating period P, thickness T, duty cycle D, or cavity length L. This property is superior to that of DBR-based FPFs, the peak tuning of which is generally achieved only by changing the cavity length directly [1] or indirectly [2]. The peak shifting in the HCG-FPF can be interpreted as a phase shift variation caused by a change in the specific structure parameters. It should be noted that the peak moves in a quasi-linear manner against L, as well as against P and T, which significantly facilitates our prediction of the peak location as the corresponding parameters change. Moreover, we can readily tune the FWHM of the peak efficiently and continuously by changing P or T and consequently tune the quality factor of the HCG-FPF. With a suitable P or T, an ultra-high quality factor (e.g., as high as 625960) is theoretically attained. This characteristic is much more attractive compared with that of a DBR-based FPF, the quality factor elevation of which generally requires inordinately additional DBR pairs, making the whole device bulkier and more costly. On the other hand, thanks to the sensitivities of the wavelength location and FWHM of the peak to P, T, D, and L, it is very probable that sensing applications of the HCG-FPF referring to these structure parameters can be exploited. A non-zero incident beam plane angle can degrade the peak transmittivity and give rise to a high sideband, because the HCG-FPF is polarization-sensitive and designed only for TE polarization; it is necessary to keep the incident beam plane angle at zero as much as possible. Oblique incidence on the HCG-FPF moves the peak toward a shorter wavelength and broadens its FWHM. This feature may be applied to sensing angle-dependent information. Nevertheless, the quality factor degrades rapidly with the increase in the incident angle; thus, oblique incidence should be avoided when the HCG-FPF is considered for ultra-high quality factor applications. This HCG-FPF is proposed for implementation on a double-SOI platform. The preserved silicon

substrate will degrade the performance of the HCG-FPF significantly by decomposing the transmission peak into a bundle of sub-peaks. The thicker the substrate is, the worse the transmission spectrum will be. Generally speaking, post-treatment of the substrate is essential to minimize or eliminate its negative effect. Structural differences (particularly in grating thickness) between the two HCGs influence the wavelength location and FWHM of the peak and, in particular, degrade the peak transmittivity. Ensuring consistency in the structure of the two HCGs during the practical fabrication process is therefore very important.

6. Conclusion

This study investigates the transmission properties of a silicon-based HCG-FPF. The HCG-FPF is proposed to be monolithically implemented on a double-SOI platform, and features ultra compactness, low weight, tunable FWHM and peak location, and easy integration with silicon-based photonic devices. We briefly discuss its feasible fabrication process. By means of RCWA simulations, the influences of various factors (grating period, thickness, duty cycle, filter cavity length, oblique incident angle, silicon substrate thickness, and structural differences between the two HCGs) on the transmission properties of the proposed filter are analyzed and discussed exhaustively. The peak location is capable of being tuned efficiently by varying the grating period, thickness, duty cycle, or filter cavity length, because of its sensitivities to these structure parameters. The FWHM of the peak is also capable of being tuned continuously by altering the grating period or thickness; thus, an ultra-high quality factor is readily achieved by merely choosing the proper period or thickness. A non-zero incident beam plane angle generally causes a decrease in peak transmittivity and a rise in side-band. A blue shift of the peak appears with an increasing oblique incident angle, which severely degrades the quality factor of the HCG-FPF. We also consider the contributions of the silicon substrate, of which an increasing thickness leads to a serious splitting of the peak. In any case, this negative effect can be considerably alleviated by substrate thickness reduction and ARC layer deposition or eliminated through complete substrate removal. Structural differences between the two HCGs may degrade the peak transmittivity, as well as change the FWHM and peak location. Thus, the structural consistency of the two HCGs should be maintained as much as possible. Overall, this study makes the peculiar transmission properties of the HCG-FPFs much more distinct, which is highly important for their practical design and applications.

References

[1] C. F. R. Mateus *et al.*, "Widely tunable torsional optical filter," *IEEE Photon. Technol. Lett.*, vol. 14, no. 6, pp. 819–821, Jun. 2002.
[2] Y. Zuo *et al.*, "A Si-based tunable narrow-band flattop filter with multiple-step-type Fabry–Pérot cavity structure," *IEEE Photon. Technol. Lett.*, vol. 17, no. 10, pp. 2134–2136, Oct. 2005.
[3] X. Duan *et al.*, "Long wavelength multiple resonant cavities RCE photodetectors on GaAs substrates," *IEEE Trans. Electron Devices*, vol. 58, no. 11, pp. 3948–3953, Nov. 2011.
[4] X. Fan *et al.*, "A novel hybrid integrated photodetector based on a cone absorption cavity," *J. Lightw. Technol.*, vol. 31, no. 8, pp. 1234–1239, Apr. 2013.
[5] P. Liu *et al.*, "An optofluidics biosensor consisted of high-finesse Fabry–Pérot resonator and micro-fluidic channel," *Appl. Phys. Lett.*, vol. 100, no. 23, Jun. 2012, Art. ID 233705.
[6] P. Liu *et al.*, "An ultra-low detection-limit optofluidic biosensor with integrated dual-channel Fabry–Pérot cavity," *Appl. Phys. Lett.*, vol. 102, no. 16, Apr. 2013, Art. ID 163701.
[7] H. S. Loka and P. W. E. Smith, "Ultrafast all-optical switching with an asymmetric Fabry–Pérot device using low-temperature-grown GaAs: Material and device issues," *IEEE J. Quantum Electron.*, vol. 36, no. 1, pp. 100–111, Jan. 2000.
[8] M. W. Pruessner, T. H. Stievater, M. S. Ferraro, and W. S. Rabinovich, "Thermo-optic tuning and switching in SOI waveguide Fabry–Pérot microcavities," *Opt. Exp.*, vol. 15, no. 12, pp. 7557–7563, Jun. 2007.
[9] X. Duan, Y. Huang, Y. Shang, J. Wang, and X. Ren, "High-efficiency dual-absorption InGaAs/InP photodetector incorporating GaAs/AlGaAs Bragg reflectors," *Opt. Lett.*, vol. 39, no. 8, pp. 2447–2450, Apr. 2014.
[10] H. Gebretsadik *et al.*, "Design and realization of a 1.55-μm patterned vertical cavity surface emitting laser with lattice-mismatched mirror layers," *J. Lightw. Technol.*, vol. 17, no. 12, pp. 2595–2604, Dec. 1999.
[11] M. C. Y. Huang, Y. Zhou, and C. J. Chang-Hasnain, "A surface-emitting laser incorporating a high index contrast subwavelength grating," *Nature Photon.*, vol. 1, no. 2, pp. 119–122, Feb. 2007.
[12] C. Lin *et al.*, "High temperature continuous-wave operation of 1.3- and 1.55-μm VCSELs with InP/Air-Gap DBRs," *IEEE J. Sel. Topics Quantum Electron.*, vol. 9, no. 5, pp. 1415–1421, Sep. 2003.

[13] M. Garrigues, J. Danglot, J. L. Leclercq, and O. Parillaud, "Tunable high-finesse InP/Air MOEMS filter," *IEEE Photon. Technol. Lett.*, vol. 17, no. 7, pp. 1471–1473, Jul. 2005.
[14] C. F. R. Mateus, M. C. Y. Huang, D. Yunfei, A. R. Neureuther, and C. J. Chang-Hasnain, "Ultrabroadban mirror using low-index cladded subwavelength grating," *IEEE Photon. Technol. Lett.*, vol. 16, no. 2, pp. 518–520, Feb. 2004.
[15] A. Ahmed, M. Liscidini, and R. Gordon, "Design and analysis of high-index-contrast gratings using coupled mode theory," *IEEE Photon. J.*, vol. 2, no. 6, pp. 884–893, Dec. 2010.
[16] V. Karagodsky *et al.*, "Monolithically integrated multi-wavelength VCSEL arrays using high-contrast gratings," *Opt. Exp.*, vol. 18, no. 2, pp. 694–699, Jan. 2010.
[17] C. Chase, Y. Rao, W. Hofmann, and C. J. Chang-Hasnain, "1550 nm high contrast grating VCSEL," *Opt. Exp.*, vol. 18, no. 15, pp. 15 461–15 466, Jul. 2010.
[18] W. Hofmann *et al.*, "Long-wavelength high-contrast grating vertical-cavity surface-emitting laser," *IEEE Photon. J.*, vol. 2, no. 3, pp. 415–422, Jun. 2010.
[19] S. Boutami *et al.*, "Highly selective and compact tunable MOEMS photonic crystal Fabry–Pérot filter," *Opt. Exp.*, vol. 14, no. 8, pp. 3129–3137, Apr. 2006.
[20] E. Bisaillon *et al.*, "High reflectivity air-bridge subwavelength grating reflector and Fabry–Pérot cavity in AlGaAs/GaAs," *Opt. Exp.*, vol. 14, no. 7, pp. 2573–2582, Apr. 2006.
[21] D. Zhao, H. Yang, Z. Ma, and W. Zhou, "Polarization independent broadband reflectors based on cross-stacked gratings," *Opt. Exp.*, vol. 19, no. 10, pp. 9050–9055, May 2011.
[22] C. P. Ho *et al.*, "Development of polycrystalline silicon based photonic crystal membrane for mid-infrared applications," *IEEE J. Sel. Topics Quantum Electron.*, vol. 20, no. 4, Jul. 2014, Art. ID 4900107.
[23] C. P. Ho *et al.*, "Two-dimensional photonic-crystal-based Fabry–Pérot etalon," *Opt. Lett.*, vol. 40, no. 12, pp. 2743–2746, Jun. 2015.
[24] M. K. Emsley, O. Dosunmu, and M. S. Ünlü, "High-speed resonant-cavity-enhanced silicon photodetectors on reflecting silicon-on-insulator substrates," *IEEE Photon. Technol. Lett.*, vol. 14, no. 4, pp. 519–521, Apr. 2002.
[25] M. G. Moharam, E. B. Grann, and D. A. Pommet, "Formulation for stable and efficient implementation of the rigorous coupled-wave analysis of binary gratings," *J. Opt. Soc. Amer. A*, vol. 12, no. 5, pp. 1068–1076, May 1995.
[26] J. H. Kim, L. Chrostowski, E. Bisaillon, and D. V. Plant, "DBR, Sub-wavelength grating, and Photonic crystal slab Fabry–Pérot cavity design using phase analysis by FDTD," *Opt. Exp.*, vol. 15, no. 16, pp. 10 330–10 339 Aug. 2007.
[27] D. Fattal, J. Li, Z. Peng, M. Fiorentino, and R. G. Beausoleil, "Flat dielectric grating reflectors with focusing abilities," *Nature Photon.*, vol. 4, no. 7, pp. 466–470, Jul. 2010.
[28] Y. Wang *et al.*, "Surface-normal emission from subwavelength GaN membrane grating," *Opt. Exp.*, vol. 22, no. 1, pp. 667–672, Jan. 2014.
[29] Z. Shi *et al.*, "Experimental observation of lateral emission in freestanding GaN-based membrane devices," *Opt. Lett.*, vol. 39, no. 16, pp. 4931–4933, Aug. 2014.
[30] Y. Wang *et al.*, "Guided-mode resonant HfO_2 grating at visible wavelength range," *IEEE Photon. J.*, vol. 6, no. 2, Apr. 2014, Art. ID 2200407.